Applied Physics B: Lasers and Optics manuscript No.
(will be inserted by the editor)

Combined scattering-referenced and co-doped aerosol phosphor thermometry using the Ce,Pr:LuAG phosphor

Joshua M. Herzog,[1] Dustin Witkowski,[1] and David A. Rothamer[1]

University of Wisconsin–Madison, Department of Mechanical Engineering, 1500 Engineering Dr., Madison, WI 53706, USA

The date of receipt and acceptance will be inserted by the editor

Abstract As a means of increasing the temperature range of high-precision measurements for aerosol phosphor thermometry (APT), the co-doped Ce,Pr:LuAG phosphor was investigated for use with simultaneous Pr^{3+}-scattering-referenced APT (SRAPT), Ce^{3+}-SRAPT, and co-doped APT techniques. Phosphor characterization was performed in a heated air jet at atmospheric pressure, and APT performance was estimated for the three simultaneous imaging techniques. A method for combining temperature measurements using a weighted average approach is discussed in detail and demonstrated via heated air jet imaging experiments. The combination of techniques results in a usable temperature range for the Ce,Pr:LuAG phosphor of 300 to at least 900 K, with better than 35 K estimated temperature precision from 500 to 900 K at a seeding density of 120 mm^{-3}, improving diagnostic precision and temperature range over that of any single APT technique using the Ce,Pr:LuAG phosphor. The combination of SRAPT and co-doped measurements may improve the temperature range and performance of other similar phosphors as well.

1 Introduction

Over the past decade, aerosol phosphor thermometry (APT) has received increasing attention due to its potential for high-precision, pressure- and composition-insensitive, simultaneous temperature and velocity imaging in combustion-relevant flows [1]. APT is advantageous compared to molecular tracer-based planar laser-induced fluroescence (PLIF) as phosphor particles are typically inert, and do not thermally decompose at high temperatures. APT uses thermographic phosphor particles seeded into the flow of interest. Following excitation with a laser sheet they emit temperature-dependent luminescence that can be collected to infer temperature. Planar Mie scattering measurements can also be performed to achieve simultaneous single-shot measurements of the temperature and velocity fields. Phosphors used for this purpose are typically composed of rare-earth-doped crystalline materials that are ground or formed into particles ranging in size from 100 nm to 10 µm in mean diameter.

The most common measurement approach used for two-dimensional gas temperature measurements has been the spectral luminescence intensity ratio (SLIR) method. The SLIR method relies on the change in emission spectrum shape with temperature for emission from a single ion [2]. A large number of phosphor compositions have been successfully applied for gas temperature imaging using this approach (*e.g.*, ZnO [3,4], Pr:YAG [5], and Eu:BAM [6–10]), as documented in the recent review article by Abram *et al.* [2]. However, due to decreasing signal and sensitivity with temperature when using a single ion, the maximum temperature and range over which high-precision single-shot measurements can be obtained is limited. In particular, single-shot measurements based on the SLIR method are currently only possible from room temperature up to a maximum of approximately 900 K [11].

The SLIR method typically collects emission in two wavelength bands. Sensitivity is maximized by limiting the range of wavelengths collected in each band at the cost of limiting the amount of signal collected. Recently, two intensity-based techniques aimed at breaking this trade-off between temperature sensitivity and signal have been reported by the authors: scattering-referenced APT (SRAPT) [12] and co-doped APT

[13,14]. Both techniques can provide high temperature sensitivity and measurement precision in adjustable temperature ranges by tailoring the phosphor composition to the desired application. The SRAPT technique compares the intensity of the phosphor luminescence to that of the elastically scattered laser light, while the co-doped technique compares the emission intensities of two independent ions within the same host material. The temperature sensitivity of both techniques is primarily a result of thermal quenching of the ion luminescence due to non-radiative processes. Both techniques allow the entire emission band of each ion to be collected, maximizing signal while not impacting the temperature sensitivity.

Unfortunately, as is the case for most APT techniques, both SRAPT and co-doped APT are limited to a moderate range of temperatures where high precision can be achieved (approximately 300 K for the phosphors used here). Range is limited, in part, due to decreasing signal levels with increasing temperature resulting from thermal quenching. Here, the co-doped and SRAPT techniques using the Ce,Pr:LuAG phosphor are combined to increase the useful single-shot temperature range by roughly a factor of two, allowing for continuous measurement from room temperature to at least 900 K. A method for combining multiple temperature imaging diagnostics using a weighted averaging approach is presented. The three simultaneous diagnostics (Pr^{3+} SRAPT, Ce^{3+} SRAPT, and Pr^{3+}-Ce^{3+} co-doped APT) are applied to uniform temperature fields to assess temperature precision. Finally, measurements are performed in an unsteady non-uniform heated air jet to highlight the improved capabilities of the combined APT approach.

2 Background

The measurements discussed here apply two relatively new techniques: scattering-referenced APT (SRAPT) [12], and co-doped APT [13]. Both techniques are ratiometric intensity based methods, where a measured luminescence intensity ratio

$$R = \frac{S_2}{S_1} \tag{1}$$

is formed between two signals S_1 and S_2. The ratio is a function of temperature, and is generally insensitive to pressure and gas composition. For co-doped APT, S_1 and S_2 are the emission intensities of the two ions.

Here, for Ce,Pr:LuAG, S_2 is the Ce^{3+} emission intensity, and S_1 is the Pr^{3+} emission intensity. For SRAPT, S_2 is the scattering intensity, while S_1 is the emission intensity of an ion. For Ce,Pr:LuAG, SRAPT can be performed using both the Ce^{3+} and the Pr^{3+} emission intensities.

Instead of spectral sensitivity, both techniques rely on thermal quenching for temperature sensitivity. The intensity of an ion's emission as a function of temperature can be approximated as [15]

$$\frac{S}{S_0} = \frac{1}{1 + C_{NR,R} \exp(-\Delta E / k_B T)} \tag{2}$$

where S_0 is the luminescence signal in the absence of non-radiative quenching, $C_{NR,R}$ is the ratio of the non-radiative attempt rate and the radiative emission rate, and ΔE is a characteristic energy gap for the quenching process. The emission intensity, and thus measured signal, decreases quickly with temperature once the second term in the denominator has a magnitude close to or greater than 1. For SRAPT, the ratio temperature sensitivity is identical to the signal temperature sensitivity for the ion, since the scattering intensity is assumed to be a constant per particle. For co-doped APT, the ratio sensitivity is equal to the difference in sensitivity for the two ions' signals.

Simultaneous co-doped and SRAPT measurements with the Ce,Pr:LuAG phosphor are possible because the emission wavelengths of the two ions and the excitation wavelength are well separated [14]. This allows for the entire emission spectrum of each ion to be captured without interference. The phosphor is excited at 266 nm, while the Pr^{3+} emission is from 300-450 nm, and the Ce^{3+} emission is from 450-700 nm. The emission lifetimes of the two ions, 21 ns for Pr^{3+} [16] and 61 ns for Ce^{3+} [17] at room temperature (neglecting any ion-ion interaction), are short enough that measurements can be made in high-speed flows.

2.1 Diagnostic performance

Diagnostic performance, including precision index and bias limit (as defined by ASME PTC-19.1-1985 [18]), can be estimated from the fractional sensitivity of the ratio calibration function. The fractional temperature

sensitivity of the ratio R is given by

$$\xi_T = \frac{1}{R}\frac{\partial R}{\partial T}, \tag{3}$$

and the temperature precision index (standard deviation) s_T is given by

$$s_T = \frac{s_R}{R\xi_T}. \tag{4}$$

where s_R is the ratio precision index (standard deviation).

Phosphor characterization for Ce,Pr:LuAG was carried out in detail previously [14] using a three-level population model with temperature-dependent ground-state absorption (GSA) and excited-state absorption (ESA) cross sections. The model was fit to Ce^{3+} and Pr^{3+} per particle luminescence intensity measurements as a function of laser fluence and temperature from 300 to 700 K, via the ESA and GSA cross-sections. While the results provide a consistent explanation for the low signal levels per ion and fluence nonlinearity commonly observed for phosphors relying on 4f5d emission for APT applications (*e.g.*, [7,19]), the main purpose was to provide a convenient physics-based temperature calibration for the co-doped APT technique. Further details on the absorption cross-section fits using the three-level model are available in Appendix B and in [14]. Experiments described here extend the applicable range of Ce,Pr:LuAG to 900 K using a combination of SRAPT and co-doped APT.

3 Materials and Methods

3.1 Experimental Setup

The experimental setup (shown in Figure 1) for the current work consisted of a heated jet at atmospheric pressure exiting from a 19-mm inner-diameter ceramic tube. The jet was seeded with Ce,Pr:LuAG thermographic phosphor particles (Phosphor Technology, 0.9 μm mean diameter based on number-weighting). Two heaters, an inline heater (Sylvania, 038825) and a vacuum forged ceramic fiber cylindrical heater (Thermcraft Inc. Fibercraft, VF-180-2-24-V), were used to control the jet center exit temperature to within a few K. The

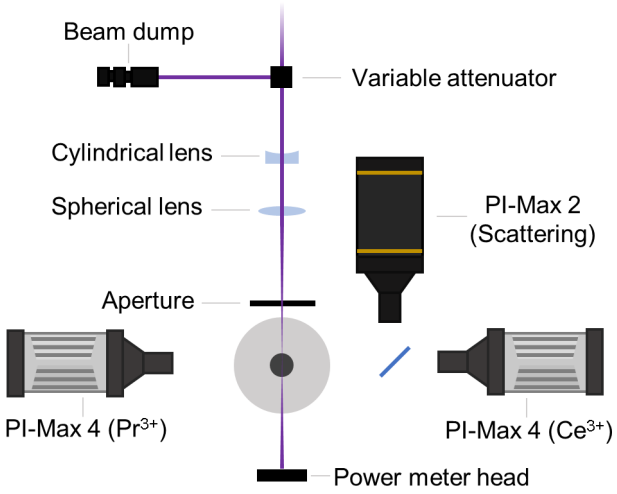

Fig. 1: Experimental setup diagram for heated jet.

setup is capable of producing either a uniform temperature jet up to 800 K, or a non-uniform temperature jet with a maximum temperature of 900 K at the edges. A type-K thermocouple was used to measure jet profiles for comparison with the APT measurements. Total uncertainty for the thermocouple measurements near the center of the jet for the uniform flow cases is estimated to be between 10 and 20 K resulting from uncorrected conduction and radiation biases. Biases near the edge, and for the non-uniform temperature case, may be larger. Thermocouple biases were estimated using the theory and data presented in [20].

The 266-nm 4^{th} harmonic output of a flashlamp pumped Nd:YAG laser (Ekspla, NL 303D-10) was used to excite the phosphor particles. Total laser energy was measured with a bench-top power meter (Newport, 1835-C power meter; Newport, 919P-050-18HP thermopile sensor) and laser sheet thickness was determined using the scanning knife edge method. Laser energy was held constant at 5.5±0.5 mJ/pulse, with typical fluence values ranging from 20 to 30 mJ/cm^2.

Luminescence emission from Ce^{3+} and Pr^{3+} was captured separately with two PI-MAX4 cameras (Princeton Instruments, PI-MAX4 1024i-HB-FG-18-P46), and the elastically scattered laser light was captured on a PI-MAX2 (Princeton Instruments, PI-MAX2 7489-0022). The collection equipment and estimated collection

Table 1: Equipment and estimated collection efficiencies for the scattering and luminescence cameras. A dichroic beamsplitter (Semrock Inc. FF347-Di01) was also used and included in the collection efficiency calculation, but is not explicitly listed in the table.

Signal	Camera	Lens	Filters	$\eta_{PC}\eta_{opt}$ [-]	$\Omega/4\pi$ [-]
Ce^{3+}	PI-Max 4	Nikon Nikkor 85-mm ($f/1.4$)	Schott Glass WG295 Asahi Spectra ZVL0470	0.37	2.5×10^{-3}
Pr^{3+}	PI-Max 4	Sodern Cerco 45-mm ($f/1.8$)	Schott WG-295 Semrock FF01-267 Melles Griot O3SWP604	0.18	1.5×10^{-3}
Scat.	PI-Max 2	Nikon Nikkor UV 105-mm ($f/4.5$)	Asahi Spectra ZUS0300 Schott WG-280	0.02	2.5×10^{-4}

efficiencies are given in Table 1. Camera filters were tilted approximately 3° to avoid imaging of rejected light.

Seeding density was measured by calibrating the measured scattering intensity at a constant laser fluence to optical extinction measurements using the 532-nm 2nd harmonic output of a continuous-wave (CW) Nd:YAG laser, and correcting the images to account for varying laser fluence. For more details on the experimental setup and the seeding density determination method, please see [14].

3.2 Experimental conditions

All experiments were performed in the atmospheric air jet. The jet was operated at a constant mass flow rate of 28.3 SLPM, corresponding to a jet exit velocity of 1.7 m/s at room temperature. The Reynolds number in the tube at room temperature was ∼2000, and the flow in the tube was not turbulent. Characterization experiments were performed after the jet is heated uniformly to a temperature of either 600 or 800 K. When

heated to 600 K, the velocity was doubled to 3.4 m/s, with a corresponding Reynolds number of ∼1300. At 800 K, the Reynolds number was reduced to around 1000.

Measurements were also performed in a non-uniformly heated jet. A smoothly varying radial temperature profile was generated by heating the jet core to around 500 K using the inline heater and strongly heating the edge of the jet with the cylindrical heater to 900 K. This produced a jet with a hot edge and colder center region resulting in a temperature range from 550 to 900 K.

3.2.1 Data processing A background correction was performed for each camera, taken with the laser off. A series of 200 background images were taken immediately before performing the experiment, after the jet was heated. The images were averaged, then subtracted from the single-shot imaging data. Images taken with the laser on but without seeding the flow revealed no significant stray light.

Following background subtraction, three different ratios were calculated on a single-shot basis: the Ce^{3+} SRAPT ratio (S_{Mie}/S_{Ce}), the Pr^{3+} SRAPT ratio (S_{Mie}/S_{Pr}) and the co-doped ratio (S_{Ce}/S_{Pr}). A series of 200 images were taken at each combination of jet exit temperature. A flatfield correction was performed on the single-shot ratio images using the average room temperature ratio, forcing the average ratio at room temperature to be one. A combination of hardware binning (4x4) and software binning (2x2) of the images resulted in the final estimated spatial resolution of 1.12 lp/mm based on processed images of a United States Air Force (USAF) 1951 resolution test chart. A mask was generated using an automated thresholding technique [21] based on the scattering intensity images; regions with scattering intensity below the threshold were masked and their ratio and temperature values were ignored in the remaining analysis.

3.3 Combined technique temperature calculation

One of the unique aspects of the current work is the combination of simultaneous methods of measuring temperature to expand the range of temperature measurements. A weighted-mean temperature is used to combine the simultaneous measurements from the different methods: Ce^{3+} SRAPT, Pr^{3+} SRAPT, and co-

doped APT. The weighted mean temperature is used as it provides several benefits over the use of a single diagnostic. As will be shown, the weighted mean approach provides a smooth and automated transition between multiple diagnostics based on single-shot temperature precision estimates, and thus results in an improved measurement that takes advantage of all available temperature data.

The weighted-mean temperature ($\bar{T}$) is defined as

$$\bar{T} = \frac{\sum_i T_i w_i}{\sum_i w_i}, \tag{5}$$

where T_i and w_i are the measured temperature and weight of technique i, respectively. Assuming that uncertainties are uncorrelated, the temperature precision of the mean ($s_{\bar{T}}$) is given by

$$s_{\bar{T}}^2 = \frac{\sum_i w_i^2 s_{T_i}^2}{\left(\sum_i w_i\right)^2}. \tag{6}$$

It can be shown that the optimum weighting is given by (see, *e.g.* [22])

$$w_i = s_{T_i}^{-2}, \tag{7}$$

which enforces the condition that $\partial s_{\bar{T}}^2 / \partial w_i = 0$ for all i[1]. The precision in the mean is then given by

$$s_{\bar{T}}^{-2} = \sum_i s_{T_i}^{-2}. \tag{8}$$

For each individual temperature measurement it is thus necessary to estimate the temperature precision, using camera and optical parameters as well as temperature sensitivity, to determine the relative weight of each diagnostic before performing the average. Temperature precision for each diagnostic can be estimated from Equation 4.

The precision in the weighted-mean temperature measurement can be further written in terms of an average ratio ($\bar{R}$), ratio precision ($s_{\bar{R}}$) and sensitivity (ξ),

$$s_{\bar{T}}^2 = \frac{s_{\bar{R}}^2}{\xi^2 \bar{R}^2}. \tag{9}$$

[1] This corresponding critical point additionally must be a minimum as $\partial^2 s_{\bar{T}}^2 / \partial w_i^2 > 0$ assuming the weightings are non-negative.

By defining the average ratio and ratio precision as

$$\frac{\bar{R}^2}{s_{\bar{R}}^2} = \sum_i \frac{R_i^2}{s_{R_i}^2} \tag{10}$$

a representative temperature sensitivity for the combined technique can be estimated as

$$\xi^{-2} = \frac{\sum_i w_i \xi_i^{-2}}{\sum_i w_i}. \tag{11}$$

The imaging results for the combined technique are determined by calculating the weighted average of the three diagnostics at each pixel location. For each diagnostic, temperature precision is estimated at each pixel using the measured (single-diagnostic) temperature and signal-to-noise ratio (SNR) for each camera based on manufacturer data according to Equation 4; in terms of signal intensity, this becomes

$$s_{T_i}^2 = \frac{s_{R_i}^2}{\xi_i^2 R_i^2} = \frac{s_{S_{1,i}}^2}{\xi_i^2 S_{1,i}^2} + \frac{s_{S_{2,i}}^2}{\xi_i^2 S_{2,i}^2} = \frac{\mathrm{SNR}_{1,i}^{-2} + \mathrm{SNR}_{2,i}^{-2}}{\xi_i^2} \tag{12}$$

where $\mathrm{SNR}_{j,i}$ is the signal-to-noise ratio of camera j for technique i. The temperature precision estimated for each method is then used to determine the relative weightings at each pixel using Equation 7. The estimated result for the combined technique is then calculated using these weights. After estimating the weighted average temperature in this way, the process is repeated using the estimated weighted average temperature in determining the new single-diagnostic precision estimates and weights. The combined result is then updated using these estimates.

4 Ratio and sensitivity results

In order to perform temperature imaging using the co-doped and SRAPT techniques, calibrations for the the associated ratios versus temperature are required. These functions are used to infer the temperature from the measured ratio in the temperature imaging experiments. For the current work the co-doped ratio, SRAPT ratio for Pr^{3+}, and SRAPT ratio for Ce^{3+} were required. Data taken in the jet with a uniform stable jet exit temperature at a constant average fluence of 25 mJ/cm^2 were used for the ratio calibrations, along with results from previous work [14]. Ratio measurements were averaged over the center 2 mm $\times$ 2 mm square of

the jet at 600 and 800 K, and a similar sized region at the non-uniform jet edge for the 900 K data point. The three-level model described earlier was used as the calibration function for both the co-doped and SRAPT techniques. The data acquired in this work extend the aerosol calibration to 900 K.

4.1 Ce^{3+} SRAPT ratio

Figure 2 displays the Ce^{3+} SRAPT ratio measurements and ratio calibration as a function of temperature. Data from previous furnace [19] and aerosol [14] measurements (25±5 mJ/cm^2 fluence) are shown along with and the current aerosol measurements. Furnace measurements were taken at a fluence of 1 ± 0.2 mJ/cm^2, for further details on those measurements please refer to [19]. Results from the current work are shown at 600 K and 800 K from the uniform jet exit temperature measurements, and at 900 K from the non-uniformly heated jet. Previous work indicated little fluence dependence in the ratio [14]. In Figure 2, the Ce^{3+} SRAPT ratio first decreases slightly with increasing temperature up to approximately 500 K. Above 500 K the ratio first slowly increases, then above 800 K increases rapidly. The ratio increases by approximately a factor of 2 over the 100 K temperature interval from 800 to 900 K. This rapid increase indicates good sensitivity to temperature for temperatures greater than $\sim$ 700 K.

The furnace data, which was not used in the model fitting, deviates slightly from the aerosol data. The observed differences are likely due to differences in absorption behavior between the bulk powder and dilute aerosol phases, as proposed by Fond *et al.* [23]. Emission intensity is proportional to the amount of laser light absorbed by the sample. In the aerosol phase, the fraction of absorbed laser light is proportional to seeding density and absorption cross-section; however, in the bulk powder phase, the relationship to absorption cross-section is expected to be weaker since penetration depth, or more generally the volume over which light is absorbed, increases as absorption cross-section is reduced (see [24] for a detailed analysis of light propagation in turbid media). As a result, the amount of light absorbed by the bulk powder sample has a reduced dependence on absorption cross-section. The furnace ratio thus does not accurately reflect changes in absorption cross-section with temperature.

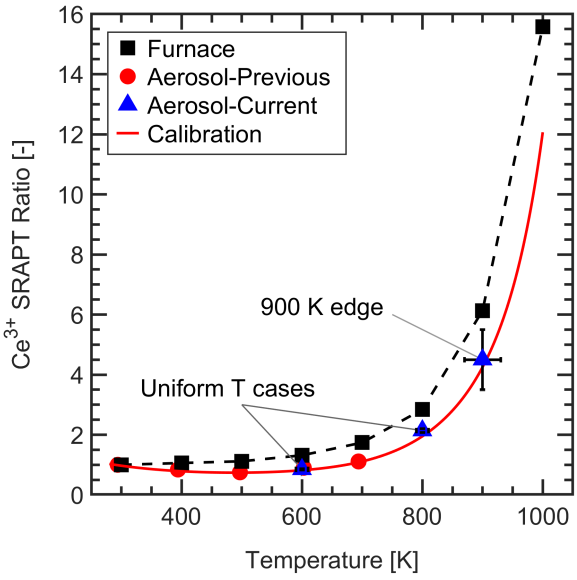

Fig. 2: Measured Ce^{3+} SRAPT ratio versus temperature. Aerosol ratios measured in the current work are shown in comparison with previous lower temperature aerosol data from [14], and high-temperature furnace calibration data from [19]. Error bars correspond to the 95% confidence interval of the mean ratio. Error bars for the 600 and 800 K data points are smaller than the symbols.

The higher temperature data points for the furnace data are useful as a reference at temperatures above 900 K where aerosol data is not currently available. Temperatures up to 900 K are to be measured in the jet, so it is necessary that the calibration extend beyond 900 K since noise will inevitably result in ratios corresponding to higher temperatures. Clipping off data with ratios corresponding to temperatures > 900 K would bias the results low.

The calibration function based on the three-level model (see Appendix A for more information on the calibration function) fits the aerosol ratio measurements well. The model and measured aerosol ratios shown in Figure 2 agree to within 5 percent at 800 K and about 1% at 600 and 900 K, neglecting the uncertainty in the 900 K temperature measurement. The physics-based calibration allows extrapolation of the ratio

to temperatures beyond where aerosol ratio measurements are currently available. Some confidence in the extrapolation is provided by the high-temperature furnace data also shown in the plot.

4.2 Pr^{3+} SRAPT ratio

Measurements of the Pr^{3+} SRAPT ratio versus temperature and the ratio calibration model fit are presented in Figure 3. The data shown includes aerosol measurement results from the current work at 600, 800, and 900 K (hot edge result), and from previous work at 700 K and lower temperatures [14]. Results shown are at a fluence of 25±5 mJ/cm^2. High-temperature furnace data from [19] are also shown. As with Ce^{3+}, the furnace data does not match the low-seeding-density aerosol measurements presented here. The relatively large differences between the furnace data and the aerosol results highlight the need to calibrate in an aerosol environment to avoid non-ideal effects present in the furnace data. The aerosol measurements from the current work agree with the previous aerosol data to within 8% (ignoring measurement uncertainty), and the trends are described well by the model. The 8% discrepancy may be a result of uncertainty in the laser fluence.

4.3 Co-doped APT ratio

The co-doped ratio is simply determined from the ratio of the Pr^{3+} SRAPT ratio and the Ce^{3+} SRAPT ratio. The resulting co-doped ratio based on the two SRAPT ratio curves is shown in Figure 4. Although the furnace data predict a monotonic increase in co-doped ratio with temperature up to 800 K, this is not the case for the aerosol measurements. The aerosol measurements are all in good agreement, with residuals of 5% or less. The high-temperature measurements at 800 and 900 K verify the double-valued nature of the aerosol co-doped ratio for Ce,Pr:LuAG.

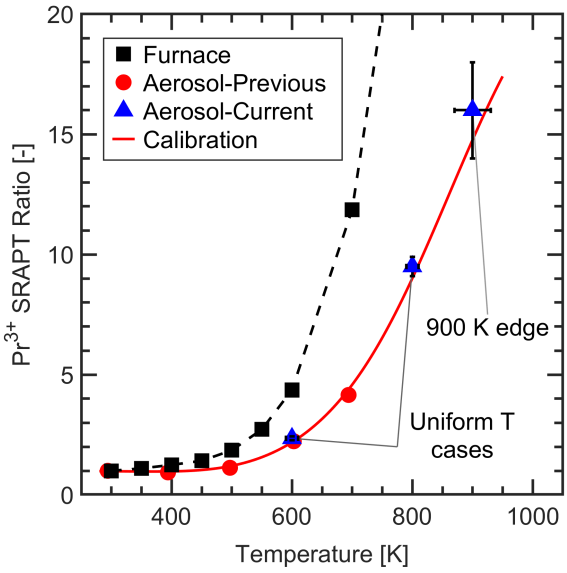

Fig. 3: Measured Pr^{3+} SRAPT ratio versus temperature. Aerosol ratios measured in the current work are shown in comparison with previous lower temperature aerosol data from [14], and high-temperature furnace calibration data from [19]. Error bars correspond to the 95% confidence interval of the mean ratio. Error bars for the 600 and 800 K data points are smaller than the symbols.

4.4 Sensitivities for all three methods

Figure 5 shows the fractional temperature sensitivity (ξ_T) for all three techniques. The Ce^{3+} SRAPT sensitivity starts off slightly negative at temperatures below approximately 500 K due to a slightly decreasing ratio that reaches a minimum at ~500 K. Above 500 K, the sensitivity is positive and at 700 K the temperature sensitivity reaches over 0.5%/K. The measured sensitivity continuously increases above the Ce^{3+} quenching temperature (T_{50}, the temperature at which the lifetime is reduced by 50%, is about 750 K for Ce^{3+}) for the range of temperatures shown here. Previous work has shown that there is little fluence-dependence in the temperature sensitivity, except at very high temperatures [14].

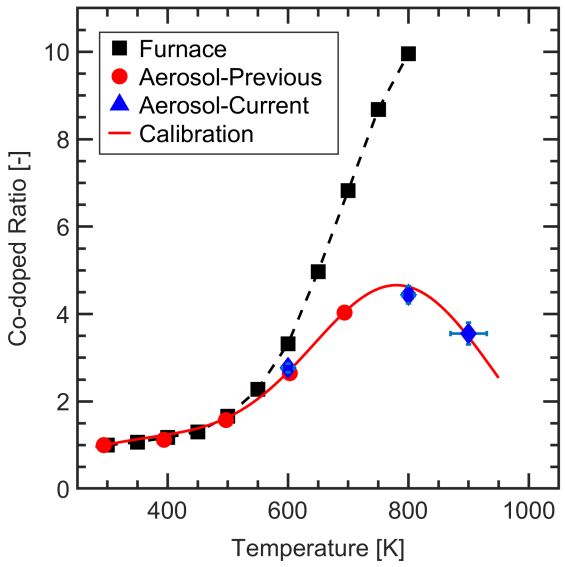

Fig. 4: Measured co-doped ratio versus temperature. Aerosol ratios measured in the current work are shown in comparison with previous lower temperature aerosol data from [14], and high-temperature furnace calibration data from [19]. Error bars correspond to the 95% confidence interval of the mean ratio. Error bars for the 600 and 800 K data points are smaller than the symbols.

The fractional temperature sensitivity for Pr^{3+} SRAPT is also shown in Figure 5. The temperature sensitivity has a peak slightly above the Pr^{3+} quenching temperature ($T_{50} \approx 550$ K for Pr^{3+}) at ~650 K. Above 650 K, the Pr^{3+} SRAPT sensitivity drops monotonically; this is expected based on Equation 2.

The co-doped sensitivity (also shown in Figure 5) has a shape similar to the Pr^{3+} SRAPT sensitivity, peaking near 600 K, but changes less with temperature below 600 K. Above 600 K, the sensitivity drops quickly because the Ce^{3+} intensity also starts to decrease. At around 800 K, the Ce^{3+} and Pr^{3+} sensitivities are the same, such that the co-doped sensitivity goes to zero. For each technique the fluence dependence is minimal based on the data presented in [14], except for a slight decrease in Pr^{3+} temperature sensitivity with increasing fluence above 600 K.

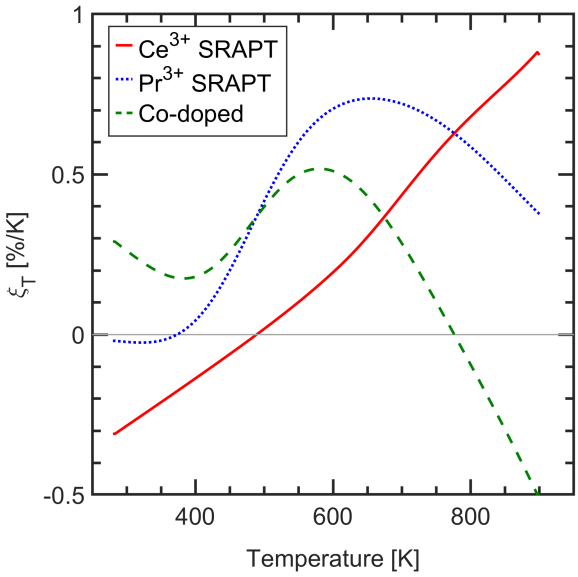

Fig. 5: Measured Ce^{3+} SRAPT, Pr^{3+} SRAPT, and co-doped temperature sensitivity versus temperature.

4.5 Combined technique sensitivity

In addition to the measurements made using the techniques individually, the three techniques are also combined in an effort to reduce total measurement uncertainty and to provide a single, improved temperature measurement over the entire calibrated temperature range. This was achieved through a weighted-average, where weights are determined according to the estimated relative temperature precision of each technique as discussed in Section 3.3.

The resulting average sensitivity, as calculated from Equation 11, is plotted in Figure 6 assuming that each ratio measurement has the same single-shot signal-to-noise ratio of 10 at 294 K. This would correspond approximately to a seeding density of 200 mm^{-3} for the current setup (see Figure 10a). For this calculation, measurements are assumed to be shot-noise-limited such that $s_{T_i}^{-2} \propto \xi_i^2 S_i$. As shown in the plot, the combined technique can achieve modest- to high-sensitivity over the entire temperature range spanning from around

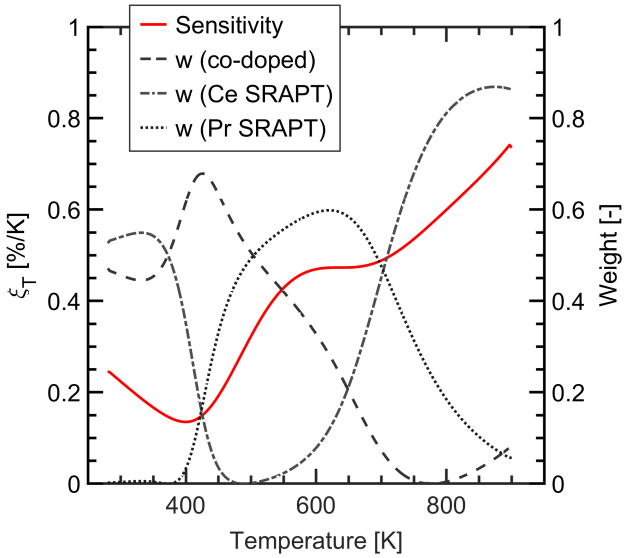

Fig. 6: Estimated temperature sensitivity of the combined co-doped/SRAPT technique with the relative weighting of each technique superimposed in dashed gray curves.

300 K up to 900 K, with a minimum fractional sensitivity of 0.13%/K at 400 K and a maximum of 0.75%/K at 900 K for the temperature range studied.

Figure 6 also shows the relative weighting of the three techniques as gray curves; at the lowest temperatures Ce^{3+} SRAPT and co-doped APT are weighted almost equally, between 400 and 500 K co-doped APT provides the most precise measurement, whereas Pr^{3+} and Ce^{3+} SRAPT become the dominant techniques at higher temperatures. Figure 6 illustrates that all three methods are needed to span the entire temperature range with reasonable sensitivity.

It is should be noted that at a given temperature, the most sensitive individual technique is more sensitive than the combined technique. This is a result of the chosen weighting which minimizes temperature uncertainty; temperature uncertainty depends on both signal intensity and temperature sensitivity.

5 SRAPT & co-doped APT imaging results

The co-doped and SRAPT techniques using Ce,Pr:LuAG were applied in two different configurations: a steady uniformly heated jet at 600 and 800 K mean exit temperatures, used to assess diagnostic performance; and an unsteady non-uniformly heated jet, used to provide a larger temperature range from 550 to 900 K in a single image. The non-uniform case is used to illustrate the capability of the combined technique in a non-uniform temperature environment. Each of the three techniques (co-doped APT, Pr^{3+} SRAPT, and Ce^{3+} SRAPT) are assessed individually for both the uniform and non-uniform case, and are compared to the results obtained by combining the three measurement methods.

5.1 Uniform temperature imaging

A series of single-shot temperature images at 300 K, and 600 and 800 K for each technique and for the combined technique, are shown in Figures 7 and 8. From the single-shot temperature images at 300 K it is clear that at the chosen measurement location (20 to 40 mm above the jet exit) some instability and vortex generation is present near the periphery of the jet. At the higher jet exit temperatures (600 and 800 K) this effect is reduced and less instability is seen in the imaged jet region as a result of the lower jet-exit Reynolds numbers when compared to the room temperature case; at 800 K, very little instability is evident in the images. The average temperature imaging results demonstrate that near the centerline of the jet the temperature is very uniform. This is also confirmed by viewing the average temperature profiles provided in Figure 9.

At 300 K, the co-doped and Ce^{3+} SRAPT techniques provide reasonable, albeit somewhat noisy measurements; none of the techniques are expected to provide high precision in this case. The lack of sensitivity at 300 K prevents any sort of reasonable measurements from being obtained for Pr^{3+} SRAPT. From Figures 3 and 5, 300 K is also near a local minimum in the Pr^{3+} technique's calibration function; thus, noise or bias

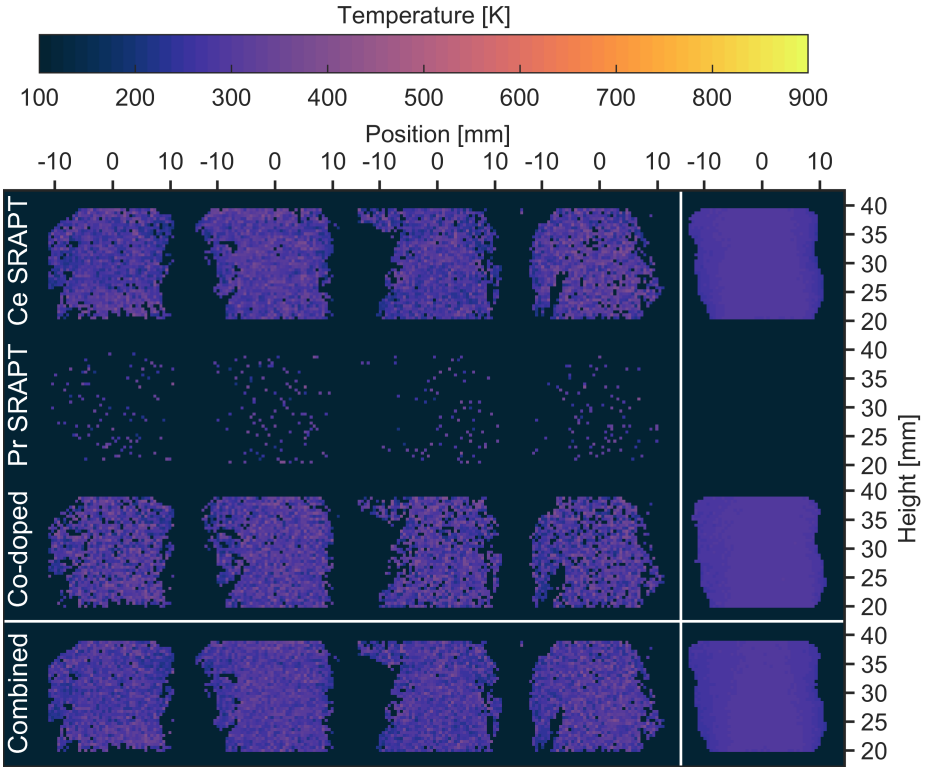

Fig. 7: Series of 4 single-shot temperature images (four leftmost columns) and 200 image average (right column) for each technique, including the combined technique, at 300 K.

that takes the measurement below a ratio of 1 cannot be converted into a temperature measurement. As a result, most of the pixels do not provide a temperature measurement.

For the 600 K jet exit temperature, Ce^{3+} SRAPT performs poorly with many pixel locations not providing temperature data and biases are seen in the average temperature results. This is due primarily to low temperature sensitivity and double-valued ratio near this temperature (see Figures 2 and 5). The single-shot imaging performance of Pr^{3+} SRAPT is reasonably good for a jet exit temperature of 600 K and the average temperature field measured appears to be of high quality with no noticeable biases. The co-doped APT results for Ce,Pr:LuAG at 600 K are intermediate in single-shot imaging performance. They show slightly

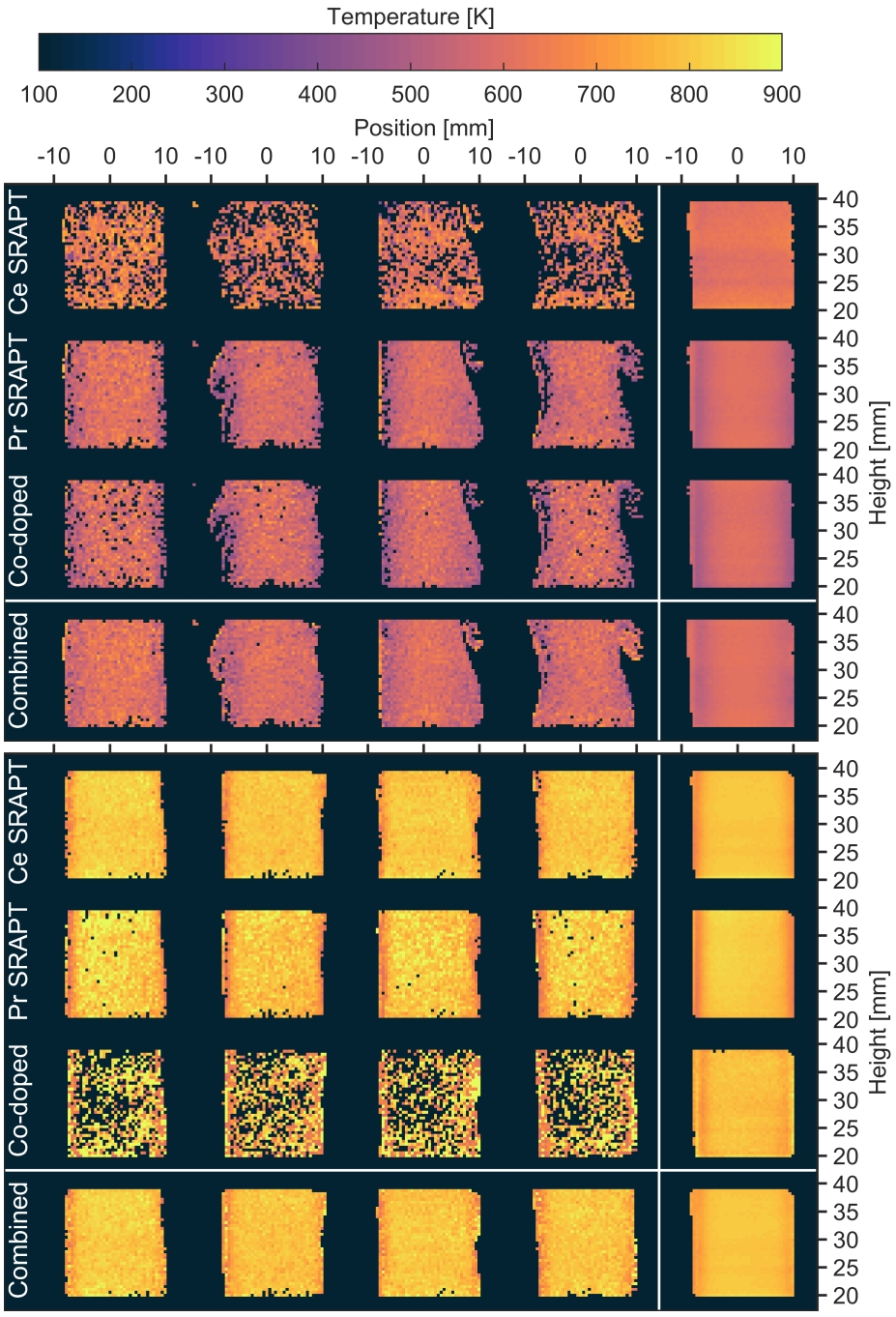

Fig. 8: Series of 4 single-shot temperature images (four leftmost columns) and 200 image average (right column) for each technique, including the combined technique, at 600 K (Top) and 800 K (Bottom) mean jet exit center temperatures.

higher noise than the Pr^{3+} SRAPT results but are significantly better than the Ce^{3+} SRAPT results as anticipated based on the relative fractional temperature sensitivities at 600 K from Figure 5.

At 800 K the performance of Ce^{3+} SRAPT improves significantly, becoming the best of the three techniques. This is predominantly a result of the high temperature sensitivity near 800 K. At the 800 K jet exit temperature the single-shot imaging performance of Pr^{3+} SRAPT appears similar to the 600 K result, with perhaps a slight increase in noise due to the reduction in signal at the the higher temperature. The co-doped technique fares the worst at 800 K and the single-shot imaging performance is significantly degraded as a result of the poor sensitivity and decreased signal in both imaging bands. The quality of the average image is also slightly impacted.

In both the 600 K and 800 K images, there appear to be artifacts from the laser sheet (in particular, the average Ce^{3+} SRAPT images). These artifacts are likely a result of fluence uncertainty or drift in laser fluence between the room-temperature reference images and the high-temperature images, as discussed in [14]. Since bias is currently not included in the weighting scheme, several of these artifacts are also visible in the combined images.

The combined technique provides results equal to or exceeding those for any of the individual techniques at all three temperatures. At the 300 K exit temperature the combined technique results are noticeably better than the individual techniques due to the reduction in pixels with missing temperature information. For both the 600 K and 800 K exit temperatures, the results for the combined technique also provide good single-shot imaging results, outperforming all of the individual techniques at both jet exit temperatures. As can be seen, the combined technique is able to provide reasonable single-shot and average image quality at all conditions.

Temperature profiles measured radially across the jet are compared to thermocouple measurements in Figure 9. The APT temperature profiles are taken as the average of the bottom two rows of the image approximately 21 mm above the jet exit; this is approximately the same height as the thermocouple. Each imaging diagnostic individually tracks the temperature profile well at 300, 600, and 800 K, with the exception

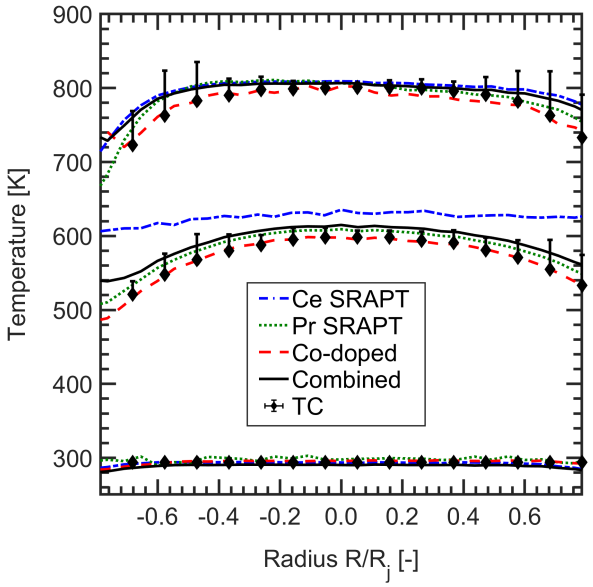

Fig. 9: Mean temperature profiles for each technique at 300, 600, and 800 K jet temperatures, with the uncorrected thermocouple and combined temperature profiles superimposed. The thermocouple error bars represent the potential uncorrected bias due to conduction and radiation.

of Ce^{3+} SRAPT at 600 K. At 800 K, some deviation is observable at the jet edge which may potentially be attributed to the effects of thermocouple bias, calibration error, and/or fluence non-uniformity.

5.1.1 Single-shot ratio and temperature precision Relative ratio and temperature precision were calculated as the coefficient of variation (COV) of the measurements within the center 2 mm × 2 mm square of the jet (centered at a height of 30 mm above the jet exit) for each single-shot image. The measured ratio and temperature COV for each image is plotted versus seeding density in Figure 10 for each diagnostic at 300 K, 600 K, and 800 K. Seeding density was determined per image using the Mie scattering intensity as described in Section 3.1. From the figure, ratios typically are measured to a precision of 20% or better largely independent of the technique or temperature, while temperature precision is strongly dependent upon the measurement technique and temperature.

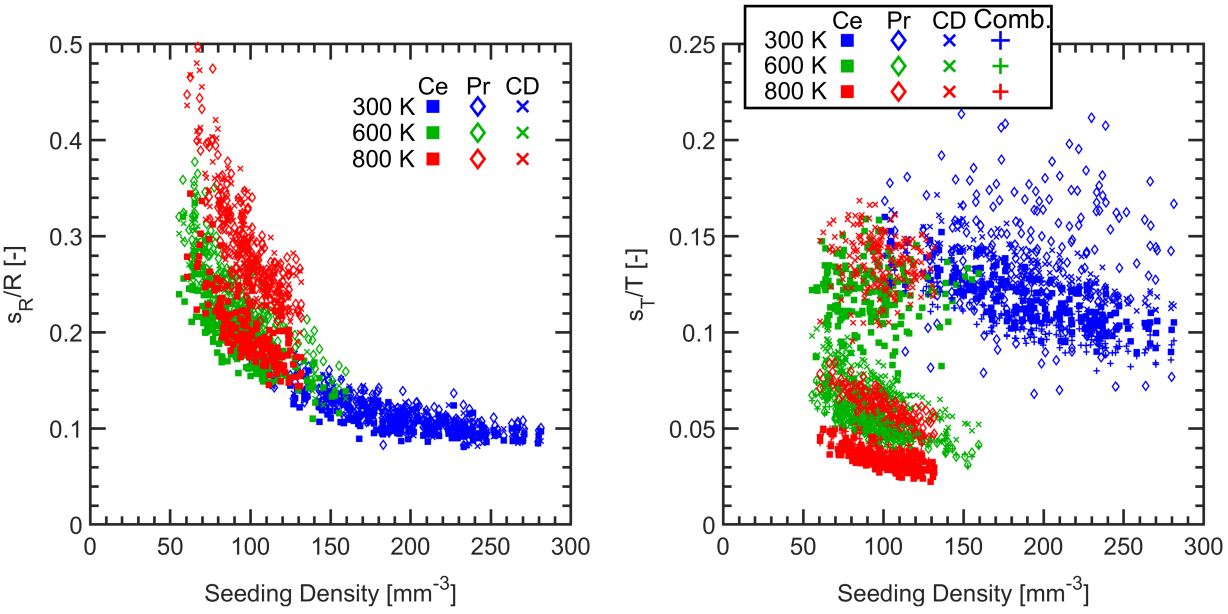

(a) Ratio

(b) Temperature

Fig. 10: Measured ratio and temperature coefficients of variation for each technique at 300, 600, and 800 K jet temperatures.

From Figure 10b, at 600 and 800 K, the combined temperature precision reaches ~20 K (3.5% and 2.5%, respectively) at the highest seeding densities (125-150 mm^{-3}), and is around 30 K on average (at 90-100 mm^{-3}). The combined precision is almost identical to that of the best technique (*i.e.*, the Ce^{3+} SRAPT technique at 800 K, and the Pr^{3+} SRAPT technique at 600 K). As expected, the precision for the combined technique is worst at 300 K, with measured precision on the order of 10% (30 K) at seeding densities of 200-250 mm^{-3}. The lower temperature precision measured at 300 K is almost entirely a result of the low temperature sensitivity. This is confirmed by studying Figure 10a, which shows that the ratio precision at 300 K is not worse than at other temperatures. At a given temperature the precision is largely dominated by whichever technique has the best precision in that temperature range. Although some individual techniques perform very poorly at a given temperature, the combined technique still does well at every temperature.

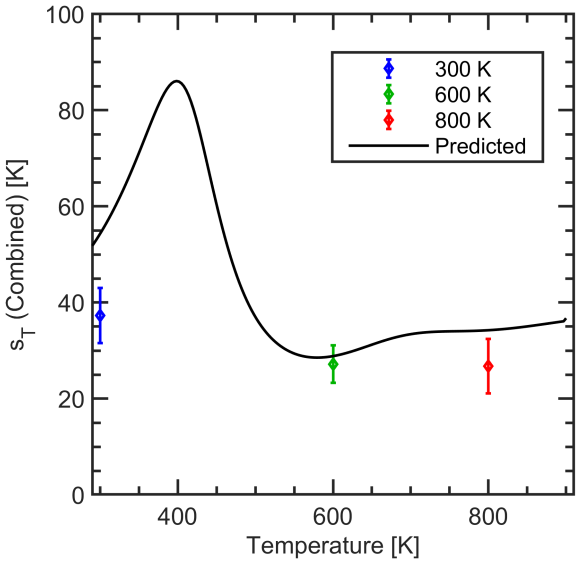

Fig. 11: Estimated precision of the combined technique from 300 to 900 K, compared with the measured precision at 300, 600, and 800 K.

The single-shot temperature precision for the combined technique was estimated based on Equation 9 using the fractional temperature sensitivities and room-temperature ratio precision measurements. The analysis assumes a constant seeding density of 120 mm^{-3} for each technique, and shot-noise limited detection. The results of this calculation are plotted as a function of temperature in Figure 11. The results indicate a relatively flat single-shot temperature precision of 35 K or better from 500 to 900 K. Below 500 K the single-shot precision gets worse due to lower temperature sensitivity for the combined technique in this temperature range (see Figure 5). The estimates correspond closely to the experimental measured values at 300, 600, and 800 K as one might expect since the estimates are based on experimental data for the sensitivity and the COV for the ratio. However, the measured precision values are slightly lower than expected at 300 and 800 K; the differences are likely due to uncertainty in the measured seeding density. Some of the discrepancy may also be a result of the nonlinear dependence of the ratio on temperature, particularly at 300 K.

5.2 Non-uniform heated jet

To help demonstrate the utility of combining techniques, the diagnostic was applied to a non-uniformly heated jet providing a range of temperatures that cannot be measured well with a single technique alone. The center temperature of the jet, as measured by thermocouple, was approximately 550 K with an edge temperature of 900 K. Based on the temperature sensitivity estimates shown in Figure 5, At 550 K the Ce^{3+} SRAPT measurement is expected to perform poorly whereas the co-doped and Pr^{3+} SRAPT measurements should perform reasonably well. At the highest temperature of 900 K, Ce^{3+} is expect to perform the best whereas co-doped APT should perform poorly and Pr^{3+} is anticipated to perform only marginally well.

A series of single-shot temperature images and 200-image averages are shown for each technique in Figure 12. The single-shot imaging results illustrate the inability of the Ce^{3+} SRAPT measurements to accurately measure the cold jet core temperature of approximately 550 K. This is due to a local minimum the ratio calibration near 500 K were the sensitivity becomes zero. Measurement noise results in a strongly bimodal temperature measurement in this region, which can be observed in the single-shot images in Figure 12, where measurements appear to alternate between 400 K and 700 K (with a mean of 550 K, the measured jet core temperature) throughout the interior of the jet. In contrast, the co-doped and Pr^{3+} SRAPT measurements have reasonable precision inside the colder jet core, but performance deteriorates near the hot jet edge due to low sensitivity.

By combining techniques, high-quality single-shot and average images are typically obtained over the entire jet profile. However, the weightings used here are estimated based on signal intensity measurements and are not perfectly representative of the relative accuracy of each measurement. In some cases this results in combined temperature measurements that are erroneously weighted in favor of a less accurate diagnostic. This can be observed in some isolated points in Figure 12. It should be noted that although temperatures measured here are limited to 900 K due to the nature of the experimental setup, we expect the Ce^{3+} SRAPT

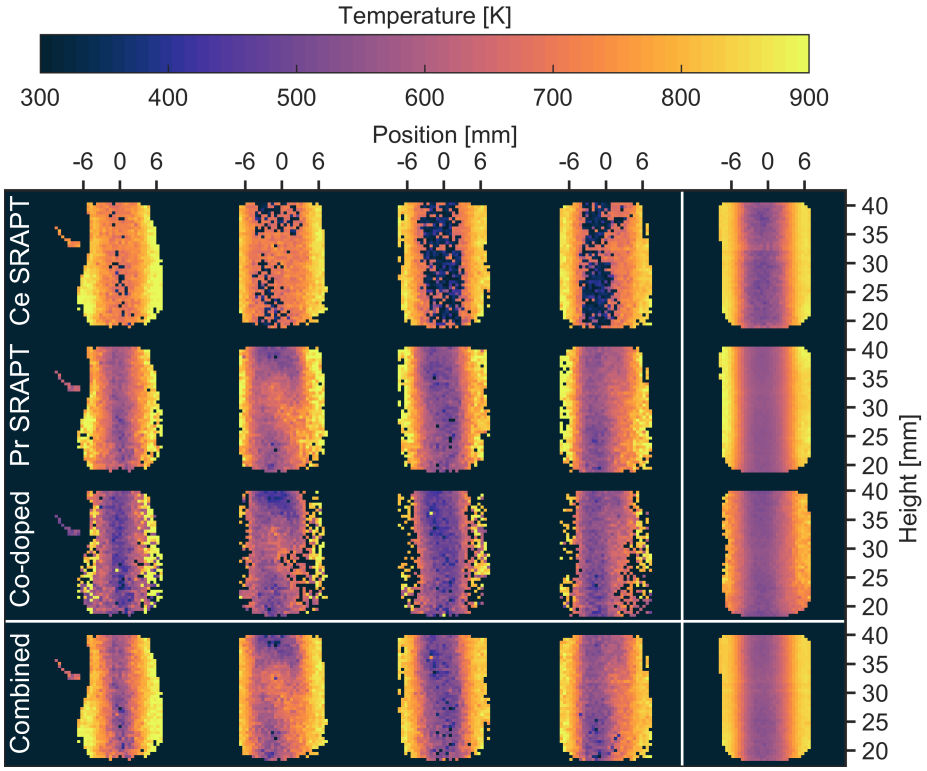

Fig. 12: Series of 4 single-shot temperature images (four leftmost columns) and 200-image average (right column) for each technique, including the combined measurement, for the unsteady heated jet.

technique (and hence the combined Ce,Pr:LuAG diagnostic) to be viable to at least 1000 K based on furnace quenching data and per particle signal level estimates [14].

Radial mean temperature profiles, calculated by averaging in the vertical direction the bottom 1 mm of the imaging data, are shown in comparison to uncorrected thermocouple measurements in Figure 13. The mean profiles of both SRAPT techniques match the thermocouple data reasonably well, although some deviation is noticeable near the highest temperatures, which may be a result of low seeding density at the edges of the jet resulting in reduced measurement accuracy. In contrast, the mean co-doped profile matches the other techniques until approximately 650 K, above which it underestimates the temperature throughout the rest of the jet. The unsteady nature of the jet, as seen in the single shot images, leads to temperature

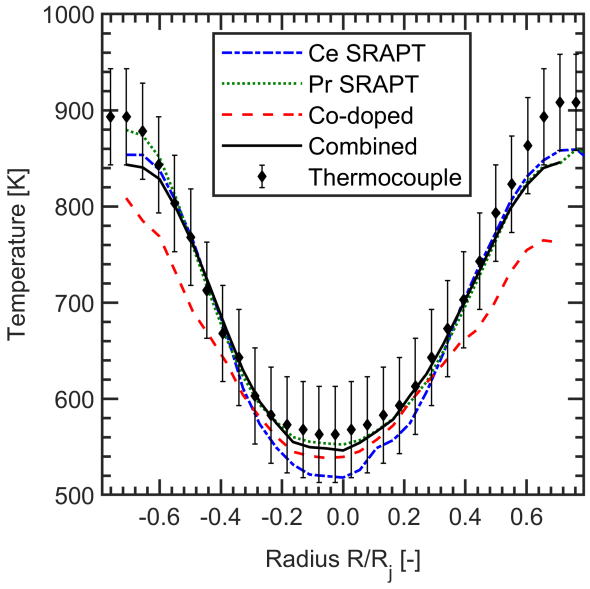

Fig. 13: Mean temperature profiles for each technique in the unsteady heated jet configuration, with the uncorrected thermocouple and combined temperature profiles superimposed. The thermocouple errorbars are taken to be 100 K to account for uncorrected biases.

fluctuations in excess of 100-200 K outside the central few millimeters of the jet. As can be seen in the single-shot images, the co-doped technique preferentially captures low temperature data due to the combined effect of Pr^{3+} thermal quenching and poor sensitivity above 700 K. This results in measurements that are biased preferentially low.

The combined temperature measurement is calculated based solely on the estimated precision for each technique. However, each diagnostic is subject to various biases that can depend on temperature and the technique used which are not included in the weighting. Ideally the weighting would minimize total uncertainty. In the future, inclusion of biases and minimization of total uncertainty could be used to further improve agreement between average profiles determined for the combined technique and reference thermocouple measurements.

5.3 Comparison with other phosphors

Several other SRAPT and co-doped techniques have been reported recently by the authors that also can potentially cover a wide temperature range. Reported characterization data from previous work was used to estimate APT performance for a variety of techniques for comparison with the Ce,Pr:LuAG phosphor and the combined methodology presented here. To ensure equivalent conditions, a fixed object-plane pixel size of 0.5 mm and seeding density of 200 mm^{-3} were used for each phosphor and technique. The calculations are performed using the method presented in [25]. For simplicity, the combined optical and quantum efficiency is held fixed at 40% for visible bands and 20% for UV bands, and particle diameters are assumed to be the same as those used here (0.9 µm by volume). The experimental values reported in Section 3.1 are used for the lens focal length, f-number, magnification, and laser sheet thickness. The results of the calculations are listed in Table 2. Cameras are assumed to be non-intensified and shot-noise limited to provide a best-case performance estimate and to avoid introducing additional error due to uncertainty in camera performance properties; this assumption is consistent with the results and analysis reported in [25]. The additional SRAPT uncertainty term, arising from the non-negligble particle size distribution width, is assumed to be constant and equal to 0.1 (see [12] for a detailed discussion and measurements of this added uncertainty).

From Table 2, a wide range of temperatures have been covered with modest precision using a variety of techniques and phosphors. The combined method with the Ce,Pr:LuAG phosphor compares favorably, and has the best performance from 500 to 800 K of any phosphor considered here. Eu:BAM SRAPT [27] and Ce:LuAG SRAPT at 355 nm excitation may have superior performance above 700 K due to the their higher emission intensity combined with good fractional temperature sensitivity.

Although the calculation was intended to provide direct comparisons, some factors vary slightly between calculations including laser fluence, integration duration, and added heat capacity. Laser fluence is taken from the characterization experiments to avoid bias in ratio and sensitivity calculations. Seeding density was

Table 2: Performance comparison of Ce,Pr:LuAG SRAPT, co-doped, and combined techniques with performance estimates for other techniques and phosphors based on recently reported data.

		Fluence	**Temperature Precision [K]**						
Phosphor	**Method**	**[mJ/cm^2]**	**500 K**	**600 K**	**700 K**	**800 K**	**1000 K**	**1200 K**	**Refs.**
Ce,Pr:LuAG	Ce^{3+}-SRAPT	30	97	25	14	12	25	-	Here
Ce,Pr:LuAG	Pr^{3+}-SRAPT	30	24	15	25	72	-	-	Here
Ce,Pr:LuAG	Co-doped	30	22	20	61	-	-	-	Here, [14]
Ce,Pr:LuAG	Combined	30	16	11	12	12	25	-	Here, [26]
Ce,Pr:CSSO	Ce^{3+} SRAPT	30	-	-	-	-	93	17	[25]
Ce,Pr:CSSO	Pr^{3+} SRAPT	30	26	20	24	33	-	-	[25]
Ce,Pr:CSSO	Co-doped	30	17	16	20	31	-	-	[25]
Ce:$GdPO_4$	Ce^{3+} SRAPT	30	-	49	52	56	25	-	[26]
Eu:BAM	Eu^{2+} SRAPT	20	15	20	21	16	16	40	[27]
Ce:LuAG	Ce^{3+} SRAPT	55	-	-	24	11	15	-	[12]

chosen to be constant to avoid bias due to differences in the additional SRAPT ratio uncertainty term (see [12]).

Although higher precision techniques have been demonstrated, with precision as small as several K or less (ZnO SLIR [3,4], or Bi:$ScVO_4$ LIR [28]), the temperature range over which these techniques can be performed is limited to within 100 K or so of room temperature. Higher temperatures are possible using Eu:BAM Eu^{2+}-SRAPT or Ce,Pr:CSSO Ce^{3+}-SRAPT, but neither of these techniques can cover the entire temperature range from 300 K to over 1000 K.

6 Conclusions

A temperature imaging technique combining co-doped APT and SRAPT was developed and implemented using the Ce,Pr:LuAG phosphor, in which three cameras are used to image the Ce^{3+}, Pr^{3+}, and scattering signals simultaneously. This work builds on the previous characterization of the co-doped Ce,Pr:LuAG technique [14] by extending the calibration range to approximately 900 K, and incorporating two scattering-referenced APT measurements which could be performed independently.

A procedure for combining the three independent temperature measurements was presented with a weighted-average approach using camera noise characteristics to estimate the relative temperature uncertainty of each measurement. The weighted-average approach results in an estimated temperature sensitivity for the combined diagnostic of between 0.1 and 0.8 %/K from room temperature to 900 K.

The combined diagnostic was applied to an atmospheric heated jet with both uniform temperature fields at 600 and 800 K and a non-uniform environment with temperatures from 500 to 900 K. From the uniform-field measurements, temperature precision of about 25 K at 600 K and 800 K mean temperatures was achieved at a seeding density of approximately 125-150 mm^{-3} and estimated spatial resolution of 1.12 lp/mm. Application of the combined technique in the non-uniform case demonstrated the capability to provide high-quality single-shot images over the entire temperature range of the jet, whereas each individual technique was only able to adequately measure a smaller portion of the jet. Average radial temperature profiles of the combined technique were shown to match thermocouple measurements to within several K over the majority of the entire temperature range. These results demonstrate the ability to achieve precise measurements over large temperature ranges through the combination of several APT techniques.

These results compare favorably with the author's recent work with Eu:BAM SRAPT and Ce:CSSO SRAPT techniques. While the upper temperature limit for Ce,Pr:LuAG is somewhat smaller than that for Eu:BAM and Ce:CSSO, similar or better temperature precision is achieved with Ce,Pr:LuAG for the same amount of thermal intrusion at temperatures below 1000 K. Unlike Eu:BAM and Ce:CSSO, the Ce,Pr:LuAG

technique discussed here is capable of covering the continuous temperature range from 300 to at least 900 K.

Acknowledgments

Research was sponsored by the Army Research Office and was accomplished under Grant Number W911NF-19-1-0238. The views and conclusions contained in this document are those of the authors and should not be interpreted as representing the official policies, either expressed or implied, of the Army Research Office or the U.S. Government. The U.S. Government is authorized to reproduce and distribute reprints for Government purposes notwithstanding any copyright notation herein.

A Ratio Calibration Function

The calibration function used in this work is based on the non-linear signal model presented in [14]. A brief overview is presented here for convenience.

The intensity of the light emitted from a phosphor particle following excitation is given by the product of the number of ions excited to the $5d$ state, n_2, and the fluorescence quantum yield (FQY), ϕ. Further, the FQY can be written as the ratio of the radiative emission rate, A, to the total deactivation rate, w, where $w = \tau^{-1}$ is the inverse of the lifetime of the excited $5d$ state. Altogether, the emitted signal in photons per ion is

$$S = n_2 A \tau. \tag{13}$$

The radiative emission rate and $5d$ lifetime can be found through time-resolved luminescence measurements; for the data presented here, the fit functions reported in [14] are used.

The excited population n_2 is determined by the absorption process in the phosphor and is dependent on both temperature and excitation laser fluence. For the purpose of diagnostic calibration, the excited

population is calculated from a simplified three-level population model with the rate equation

$$\frac{\partial}{\partial t}\begin{bmatrix} n_1 \\ n_2 \\ n_3 \end{bmatrix} = \begin{bmatrix} -\sigma_{12}\dot{\phi}'' & w_{21} & 0 \\ \sigma_{12}\dot{\phi}'' & -w_{21}-\sigma_{23}\dot{\phi}'' & 0 \\ 0 & \sigma_{23}\dot{\phi}'' & 0 \end{bmatrix}\begin{bmatrix} n_1 \\ n_2 \\ n_3 \end{bmatrix}, \tag{14}$$

where n_i is the population in level i, $w_{21} = w = \tau^{-1}$ is the deactivation rate constant, σ_{12} is the GSA cross-section, σ_{23} is the ESA cross-section, and $\dot{\phi}''$ is the laser fluence rate. Equation 14 can be solved either numerically or analytically (see the appendix in [14]) for a known fluence rate. For simplicity, the fluence rate is taken to be a constant ($\dot{\phi}'' = \phi''/\tau_{pulse}$ where τ_{pulse} is the laser pulse duration of ≈ 5 ns), and the excited population is taken at the end of the laser pulse. These approximations are valid for a laser pulse duration small compared to the phosphor lifetime; for cases where the phosphor lifetime is comparable or smaller than the laser pulse duration, the best-fit absorption cross-sections are nonphysical.

B Ground-state absorption cross-sections

The GSA cross sections and curve fit from 300 to 900 K are provided in Figure 14. The results here are strictly used for diagnostic calibration. For example, the observed GSA cross section temperature-dependence for Pr^{3+} above 700 K is nonphysical due to the model assumption that the luminescence intensity is proportional to the emission lifetime of the phosphor (*i.e.*, the emission is much longer than the laser pulse) [14], which is not satisfied at these temperatures. The cross-section fits were not altered for Pr^{3+} in this case, as the predictions fall within the uncertainty bands of the new data and because the Pr^{3+} SRAPT and co-doped techniques are primarily used for temperatures below 800 K. For Ce^{3+}, a piece-wise model was used to smoothly connect the low-temperature data (up to 600 K) to a constant value at and above 900 K. Between 600 K and 900 K, a polynomial patching function is used to enforce a continuous second derivative in log space (*i.e.*, $\ln\sigma = \sum_i a_i T^i$); below 800 K, there is only minimal difference in the fit values. As mentioned previously [14], the complicated population dynamics for Ce^{3+} at 266 nm excitation make interpretation of

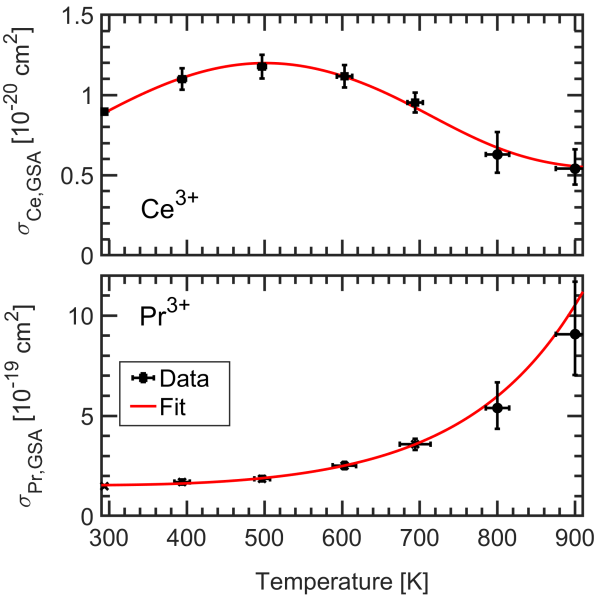

Fig. 14: Measured Ce^{3+} (top) and Pr^{3+} (bottom) GSA cross-sections (points) and best-fit function (red curve).

the results beyond the scope of the current work. The ESA fits were not modified as they had negligible observable temperature dependence up to 700 K [14].

References

1. A. Omrane, P. Petersson, M. Alden, and M. A. Linne, "Simultaneous 2D flow velocity and gas temperature measurements using thermographic phosphors," *Applied Physics B-Lasers and Optics*, vol. 92, no. 1, pp. 99–102, 2008.
2. C. Abram, B. Fond, and F. Beyrau, "Temperature measurement techniques for gas and liquid flows using thermographic phosphor tracer particles," *Progress in Energy and Combustion Science*, vol. 64, pp. 93–156, 2018.
3. C. Abram, B. Fond, and F. Beyrau, "High-precision flow temperature imaging using ZnO thermographic phosphor tracer particles," *Optics express*, vol. 23, no. 15, pp. 19453–19468, 2015.

4. L. Fan, Y. Gao, A. Hayakawa, and S. Hochgreb, "Simultaneous, two-camera, 2D gas-phase temperature and velocity measurements by thermographic particle image velocimetry with ZnO tracers," *Experiments in Fluids*, vol. 58, no. 4, p. 34, 2017.

5. N. J. Neal, J. Jordan, and D. Rothamer, "Simultaneous measurements of in-cylinder temperature and velocity distribution in a small-bore diesel engine using thermographic phosphors," *SAE International Journal of Engines*, vol. 6, no. 1, pp. 300–318, 2013.

6. J. Van Lipzig, M. Yu, N. Dam, C. Luijten, and L. de Goey, "Gas-phase thermometry in a high-pressure cell using $BaMgAl_{10}O_{17}$:Eu as a thermographic phosphor," *Applied Physics B*, vol. 111, no. 3, pp. 469–481, 2013.

7. B. Fond, C. Abram, and F. Beyrau, "Characterisation of the luminescence properties of BAM:Eu^{2+} particles as a tracer for thermographic particle image velocimetry," *Applied Physics B*, vol. 121, no. 4, pp. 495–509, 2015.

8. H. Lee, B. Böhm, A. Sadiki, and A. Dreizler, "Turbulent heat flux measurement in a non-reacting round jet, using BAM:Eu^{2+} phosphor thermography and particle image velocimetry," *Applied Physics B*, vol. 122, no. 7, p. 209, 2016.

9. A. O. Ojo, B. Fond, C. Abram, B. G. Van Wachem, A. L. Heyes, and F. Beyrau, "Thermographic laser doppler velocimetry using the phase-shifted luminescence of BAM:Eu^{2+} phosphor particles for thermometry," *Optics Express*, vol. 25, no. 10, pp. 11833–11843, 2017.

10. M. Stephan, F. Zentgraf, E. Berrocal, B. Albert, B. Böhm, and A. Dreizler, "Multiple scattering reduction in instantaneous gas phase phosphor thermometry: applications with dispersed seeding," *Measurement Science and Technology*, vol. 30, no. 5, p. 054003, 2019.

11. Z. Yin, B. Fond, G. Eckel, C. Abram, W. Meier, I. Boxx, and F. Beyrau, "Investigation of BAM:Eu^{2+} particles as a tracer for temperature imaging in flames," *Combustion and Flame*, vol. 184, pp. 249–251, 2017.

12. D. Witkowski and D. A. Rothamer, "Scattering referenced aerosol phosphor thermometry," *Measurement Science and Technology*, vol. 30, no. 4, p. 044003, 2019.

13. D. Witkowski and D. A. Rothamer, "A novel strategy to improve the sensitivity of aerosol phosphor thermometry using co-doped phosphors," *Proceedings of the Combustion Institute*, vol. 37, no. 2, pp. 1393–1400, 2019.

14. J. M. Herzog, D. Witkowski, and D. A. Rothamer, "Characterization of the Ce,Pr:LuAG phosphor for co-doped aerosol phosphor thermometry," *Journal of Luminescence*, vol. 229, p. 117665, 2021.

15. P. Dorenbos, "Thermal quenching of Eu^{2+} 5d–4f luminescence in inorganic compounds," *Journal of Physics: Condensed Matter*, vol. 17, no. 50, p. 8103, 2005.

16. T. Yanagida, Y. Fujimoto, K. Kamada, D. Totsuka, H. Yagi, T. Yanagitani, Y. Futami, S. Yanagida, S. Kurosawa, Y. Yokota, *et al.*, "Scintillation properties of transparent ceramic Pr:LuAG for different Pr concentration," *IEEE Transactions on Nuclear Science*, vol. 59, no. 5, pp. 2146–2151, 2012.

17. W. Chewpraditkul, L. Swiderski, M. Moszynski, T. Szczesniak, A. Syntfeld-Kazuch, C. Wanarak, and P. Limsuwan, "Scintillation properties of LuAG:Ce, YAG:Ce and LYSO:Ce crystals for gamma-ray detection," *IEEE Transactions on Nuclear Science*, vol. 56, no. 6, pp. 3800–3805, 2009.

18. American Society of Mechanical Engineers, "Asme ptc 19.1-1985: Measurement uncertainty," standard, American Society of Mechanical Engineers, New York, 1985.

19. D. Witkowski, J. Herzog, and D. A. Rothamer, "High-precision aerosol phosphor thermometry with Ce^{3+} and Pr^{3+} co-doped into lutetium aluminum garnet," *11th U.S. National Combustion Meeting*, 2019.

20. V. Hindasageri, R. Vedula, and S. Prabhu, "Thermocouple error correction for measuring the flame temperature with determination of emissivity and heat transfer coefficient," *Rev. Sci. Instrum.*, vol. 84, no. 2, p. 024902, 2013.

21. N. Otsu, "A threshold selection method from gray-level histograms," *IEEE transactions on systems, man, and cybernetics*, vol. 9, no. 1, pp. 62–66, 1979.

22. J. Mandel, *The statistical analysis of experimental data.* Courier Corporation, 2012.

23. B. Fond, C. Abram, M. Pougin, and F. Beyrau, "Characterisation of dispersed phosphor particles for quantitative photoluminescence measurements," *Optical Materials*, vol. 89, pp. 615–622, 2019.

24. S. T. Flock, M. S. Patterson, B. C. Wilson, and D. R. Wyman, "Monte carlo modeling of light propagation in highly scattering tissues. i. model predictions and comparison with diffusion theory," *IEEE Transactions on Biomedical Engineering*, vol. 36, no. 12, pp. 1162–1168, 1989.

25. J. M. Herzog, D. Witkowski, and D. A. Rothamer, "Characterization of ce: Csso, pr: Csso, and co-doped ce, pr: Csso phosphors for aerosol phosphor thermometry," *Measurement Science and Technology*, vol. 32, no. 5, p. 054008, 2021.

26. J. M. Herzog, D. Witkowski, and D. A. Rothamer, "Combustion-relevant aerosol phosphor thermometry imaging using ce, pr: Luag, ce: Gdpo4, and ce: Csso," *Proceedings of the Combustion Institute*, 2020.

27. D. Witkowski, J. M. Herzog, and D. A. Rothamer, "Combustion-relevant temperature imaging with scattering referenced aerosol phosphor thermometry applied to eu: Bam," *Combustion and Flame*, vol. 224, pp. 233–238, 2021.

28. C. Abram, I. W. Panjikkaran, S. N. Ogugua, and B. Fond, "Scvo 4: Bi 3+ thermographic phosphor particles for fluid temperature imaging with sub- c precision," *Optics Letters*, vol. 45, no. 14, pp. 3893–3896, 2020.